

See discussions, stats, and author profiles for this publication at: <https://www.researchgate.net/publication/49852284>

Theoretical Understanding of Ruthenium(II) Based Fluoride Sensor Derived from 4,5-Bis(benzimidazol-2-yl)imidazole (H(3)ImBzim) and Bipyridine: Electronic Structure and Binding Natu...

ARTICLE in THE JOURNAL OF PHYSICAL CHEMISTRY A · FEBRUARY 2011

Impact Factor: 2.69 · DOI: 10.1021/jp1088383 · Source: PubMed

CITATIONS

21

READS

15

5 AUTHORS, INCLUDING:



Jian Wang

Jilin University

66 PUBLICATIONS 188 CITATIONS

SEE PROFILE



Fu-Quan Bai

Jilin University

124 PUBLICATIONS 435 CITATIONS

SEE PROFILE

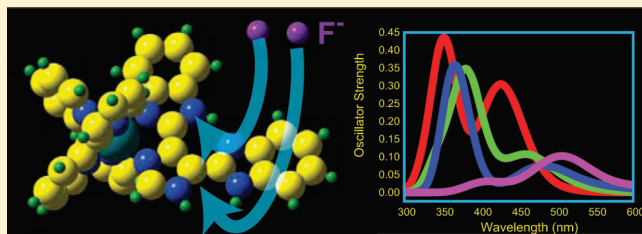
Theoretical Understanding of Ruthenium(II) Based Fluoride Sensor Derived from 4,5-Bis(benzimidazol-2-yl)imidazole (H₃ImBzim) and Bipyridine: Electronic Structure and Binding Nature

Jian Wang,[†] Fu-Quan Bai,[†] Bao-Hui Xia,^{*,†,‡} Lei Sun,[†] and Hong-Xing Zhang^{*,†}

[†]State Key Laboratory of Theoretical and Computational Chemistry, Institute of Theoretical Chemistry, Jilin University, Changchun 130023, People's Republic of China, and

[‡]College of Chemistry, Jilin University, Changchun 130000, People's Republic of China

ABSTRACT: Using density functional theory (DFT) approach, we assessed the newly developed fluoride sensor: [(bpy)₂Ru(H₃ImBzim)]²⁺ (denoted as **1**, where H₃ImBzim = 4,5-bis(benzimidazol-2-yl)imidazole and bpy = 2,2'-bipyridine). On the basis of our benchmark test, a PBE0 functional with a LanL2DZ basis set was chosen to explore the electronic structure of **1** in both ground and singlet excited states in acetonitrile solution. Both absorption bands at 426 and 352 nm are assigned as metal-to-ligand charge-transfer transition characters. By analyzing the difference of absorption spectrum between the binding adducts and the experimental measurement, the fluoride detection process was found to be driven by the proton transfer model, which makes **1** not only capable of detecting fluoride, but also for other Brønsted base anions. And the result is in general accordance with the experimental observations. We hope the current exploration can give some knowledge about the detection mechanism of the F[−] anion sensor and provide some inspiration for the design of functional molecular detectors for F[−] anion.

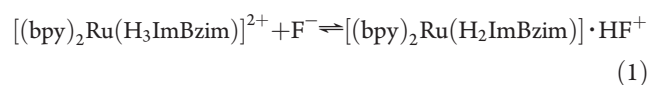


INTRODUCTION

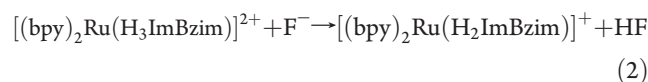
The recognition and sensing of fluoride anions has recently emerged as a key research interest because of the important role played by fluoride anion in biological process and daily life.^{1–12} Among the range of biologically important anions, fluoride is of particular interest due to its established role in preventing dental caries and as a treatment for osteoporosis.^{13–15} In daily life, fluoride is often added to drinking water and toothpaste due to its positive effects in dental health. Chronic exposure to a less salubrious level of fluoride anion, however, can lead to dental or even skeletal fluorosis, a type of fluoride toxicity that generally manifests itself clinically in terms of increasing bone density. This diversity of function, both positive and negative, makes the problem of fluoride anion detection one of considerable current interest. Given this complexity, extensive interest has been dedicated to the discovery of improved analytical methods and new sensors for detection of fluoride.^{16–20} In this regard, the transition-metal complex can be profitably used as a structural element either for building up receptors or for assisting anion binding interactions due to their relatively long lifetimes as compared to the purely organic sensor.^{10,21–23} Very recently, Saha et al.²⁴ synthesized and characterized a novel colorimetric sensor, [(bpy)₂Ru(H₃ImBzim)]²⁺, (denoted as **1** hereafter, H₃ImBzim = 4,5-bis(benzimidazol-2-yl)imidazole and bpy = 2,2'-bipyridine, see Figure 1), with visual recognition for F[−].

It must be mentioned that H₃ImBzim contains three imidazole NH protons that could act as receptors for hydrogen bonding to the anions. Theoretically, there are two possible models which master the fluoride capture process of the H₃ImBzim-based

colorimetric sensors.⁹ The first one, the hydrogen-bonding model, that is the F[−] anion, is linked to the complex via initial hydrogen-bonding interaction between the NH protons of the coordinated H₃ImBzim ligand and the anions, to form a [(bpy)₂Ru(H₂ImBzim)]·HF⁺ association complex,²⁴ which can be expressed as follows:



While the second one, proton transfer model, that is, the NH protons are deprotonated completely then the H⁺ is transferred to the Brønsted base anion, which can be expressed as follows:



Therefore, a proton-transfer based process is controlled by several factors including the acidity of the sensor, the basicity of the anion, and the stability of the conjugate base, and all of these are solvent-dependent.

A previous work claimed that all hydrogen bonds can be considered as incipient proton-transfer reactions, and for strong hydrogen bonds, this reaction can be in a very advanced state.²⁵ But for a selective fluoride sensor, it should mainly interact with the

Received: September 16, 2010

Revised: November 17, 2010

Published: February 22, 2011

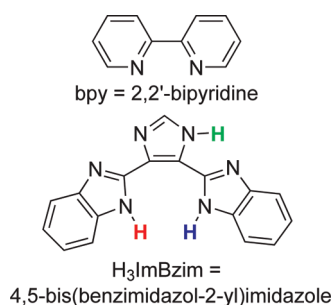


Figure 1. Ligands in current study.

fluoride anion via the formation of the appointed $F \cdots H$ hydrogen bonding.²⁶ Otherwise, the detecting signal would be interfered with by other Brønsted base anions, such as AcO^- and $H_2PO_4^-$. Since both detecting models can create a similar signal, that is, the observed color change, it may not be easy to identify which model is really responsible for the experimental color change signal when the newly developed colorimetric sensor, **1**, is used as a fluoride sensor.

In the present work, we investigated the structure and electronic properties of **1** with a theoretical approach in order to find out the exact mechanism that really controls the observed color change process. First, we had a detailed discussion on the properties of the vertical excitation absorption of **1**. Then the affections upon absorption spectra caused by hydrogen-bonding and proton-transfer process were explored, respectively. By comparing the simulated absorption spectrum with the experimental observation, the sensing nature of **1** was determined.

COMPUTATIONAL DETAILS

All calculations have been performed with the Gaussian09 program package²⁷ at the hybrid density functional theory (DFT)^{28,29} level in acetonitrile medium with tight thresholds (conver = 8) for both gradient and wave function convergence. More precisely, the PBE0^{30–32} hybrid exchange correlation (xc) functional, casting 25% of the exact Hatree–Fock exchange into the PBE xc functional, has been used throughout. This hybrid functional has been chosen due to its nonempirical nature and the benchmark test performed in the current investigation. The nature of each stationary point has been verified by harmonic vibrational frequency calculations.

In terms of basis sets, two groups were used in the current investigation. In basis set I, the double- ζ quality LanL2DZ basis sets have been used for all atoms, which makes use of the Los Alamos effective core potential (ECP)^{33–35} for inner electron core of the Ru(II) atom and the D95 V basis set for the other lighter atoms. All of the (TD)-DFT data reported in the current investigation are assessed with a fairly large basis set (basis set II): a Stuttgart relativistic small-core effective potential^{36–38} for Ru with its basis augmented by an extra f polarization function³⁹ with an exponent of 0.96, a triplet- ζ plus polarization basis set (cc-pVTZ)⁴⁰ was used for the C and N atoms, and a double- ζ plus polarization basis set (cc-pVDZ)⁴⁰ was used for H atoms.

To compute the UV–vis transition of the Ru-based compounds studied here, the singlet excited state geometry corresponding to the vertical excitations were optimized using the (PCM-) time-dependent DFT (TDDFT)^{41–43} scheme starting with the ground state geometry. The excitation energies, computed within the acetonitrile solvent simulated by the PCM

model,^{44–46} has been determined by using the so-called nonequilibrium approach, which has been designed for the study of the absorption process.^{47,48} Only singlet–singlet transitions, that is, the spin-allowed transitions, have been taken into account. Moreover, only transitions with non-negligible oscillator strengths ($f \geq 0.02$) are reported and discussed. On the base of the TDDFT computations, the spectra were afterward simulated, using GaussSum program,⁴⁹ Rev. 2.2, with the fwhm value of 1500 cm^{-1} , in order to have a direct comparison with the experimental spectra and get the simulated absorption maxima.

RESULTS AND DISCUSSION

Methodology. A crucial step in theoretical investigations employing DFT is the choice of an appropriate exchange–correlation functional and a reasonable basis set.⁵⁰ In light of recent studies and the growing use of DFT methods for computational electronic states,^{51–55} it is important to investigate their suitability for studying transition metal complexes and, if necessary, identify low-cost alternative methods. To this end, in the present work, we examined the accuracy of two DFT methods, which provided favorable applications in heavy atom molecules and weak interaction, for studying the sensing nature of **1**. Thus, complex **1** was selected to do the benchmark test with the well-established hybrid functionals Becke3–Lee–Yang–Parr (B3LYP)^{56,57} and PBE0. The optimized ground state geometry data are reported in Table 1. On the one hand, it is necessary to optimize the geometry of **1** in solution. No matter which functional is adopted, the data computed in acetonitrile solution are in better agreement with the experimental value than those obtained in gas phase. On the other hand, the PBE0 functional provides a higher accuracy (little δ , see Table 1) in the prediction of bond length and angle than B3LYP does whatever the computation was performed in acetonitrile solution or gas phase. Furthermore, as reported in Table 2, larger basis set gives out more accurate estimation of bond length but no obvious improvement in bond angles. Therefore, the results discussed in the following sections are based on the computation with PBE0 functional and larger basis set (basis set II, as indicated in Table 2) in acetonitrile solution unless otherwise indicated.

The Ground State Geometry. The main optimized structural parameters in the singlet ground state together with the X-ray crystal diffraction data²⁴ of **1** are summarized in Table 1. The optimized structure of **1** is illustrated in Figure 2, together with the corresponding label scheme.

As depicted in Figure 2, the reference molecule **1** adopts a distorted octahedral coordination geometry, wherein the N1, N2, N3, N4, N5, and N6 atoms are arranged around the Ru(II) center, defining the vertices of the octahedron. The distortion octahedron is evidenced by the bond angle $N3-Ru-N6$, 174.4° and $N4-Ru-N5$, 77.9° as well as the different bond lengths between the Ru(II) and the coordinated N atoms of the ligands. Furthermore, it can be seen that the optimized bond length and pincer angle in the singlet ground state are in general agreement with the corresponding experimental values of **1**. The calculated bond distances of Ru–N are overestimated by about $0.005 - 0.027\text{ Å}$, except that of Ru–N6 is underestimated by 0.019 Å . The discrepancy of the geometry structural data between the calculated and measured values is reasonable and acceptable, since the chemical environments of the complex are different in the two cases: in the latter case, the molecule is in a tight crystal

Table 1. Optimised Geometry Parameters of 1 in Ground State: Percent Error (δ) vs xc Functionals

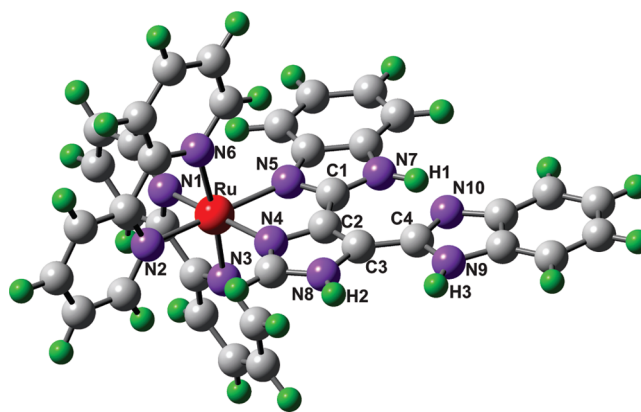
item	expt. ^a	gas phase				CH ₃ CN			
		B3LYP	δ	PBE0	δ	B3LYP	δ	PBE0	δ
bond length, Å									
Ru–N1	2.040	2.083	2.08	2.062	1.09	2.080	1.95	2.055	0.74
Ru–N2	2.033	2.088	2.73	2.058	1.21	2.082	2.39	2.056	1.14
Ru–N3	2.039	2.094	2.68	2.066	1.31	2.090	2.46	2.065	1.25
Ru–N4	2.093	2.131	1.84	2.108	0.72	2.122	1.40	2.094	0.05
Ru–N5	2.078	2.137	2.86	2.102	1.15	2.139	2.98	2.110	1.56
Ru–N6	2.074	2.093	0.88	2.068	0.29	2.090	0.76	2.064	0.50
H1–N10	2.096	1.840	12.2	1.800	14.1	1.850	11.3	1.808	13.7
bond angle, deg									
N1–Ru–N3	79.2	78.6	0.74	78.9	0.40	78.7	0.65	79.0	0.26
N2–Ru–N6	78.9	78.6	0.36	78.9	0.10	78.7	0.22	79.0	0.18
N4–Ru–N5	78.4	78.1	0.43	78.5	0.11	78.0	0.56	78.4	0.00
N1–Ru–N2	89.2	90.0	0.88	89.8	0.70	90.2	1.09	90.0	0.94
N3–Ru–N5	89.5	88.3	1.41	88.1	1.58	88.6	1.03	88.1	1.61
N6–Ru–N4	86.7	88.4	1.95	87.8	1.30	88.2	1.78	87.9	1.42
N3–Ru–N6	175.3	174.3	0.60	174.8	0.33	174.2	0.63	174.8	0.33
^a See ref 24.									

^a See ref 24.**Table 2. Optimized Geometry Parameters in Ground State: Percent Error (δ) vs Basis Set^a**

item	expt. ^b	basis set I ^c		basis set II ^d	
		cal.	δ	cal.	δ
bond length, Å					
Ru–N1	2.040	2.055	0.74	2.045	0.24
Ru–N2	2.033	2.056	1.14	2.045	0.59
Ru–N3	2.039	2.065	1.25	2.056	0.81
Ru–N4	2.093	2.094	0.05	2.088	0.23
Ru–N5	2.078	2.110	1.56	2.105	1.32
Ru–N6	2.074	2.064	0.50	2.055	0.93
H1–N10	2.096	1.808	13.7	1.886	10.0
bond angle, deg					
N1–Ru–N3	79.2	79.0	0.26	78.7	0.65
N2–Ru–N6	78.9	79.0	0.18	78.8	0.07
N4–Ru–N5	78.4	78.4	0.00	77.9	0.65
N1–Ru–N2	89.2	90.0	0.94	90.3	1.22
N3–Ru–N5	89.5	88.1	1.61	88.3	1.37
N6–Ru–N4	86.7	87.9	1.42	88.1	1.64
N3–Ru–N6	175.3	174.8	0.33	174.4	0.53

^a All computations are done with PBE0 functional in CH₃CN solution.^b See ref 24. ^c The LanL2DZ for all atoms and the corresponding ECP for Ru atom. ^d The large basis set: Stuttgart for Ru atom; cc-pVTZ for C and N atoms; cc-pVDZ for H atoms.

lattice, whereas in our simulation, the molecule is restricted in the solvent reaction field. It should be noted that strong hydrogen-bond interactions exist in this molecular system, since the distance between H1 and N10 is 1.886 Å which is less than the sum of van der Waals radius of H and N atoms (H, 1.20 Å, N, 1.55 Å) and larger than the normal N–H bond length (N–H bond length, \sim 1.00 Å).⁵⁸ And because of the strong interaction

**Figure 2.** Optimized structure and labeling scheme of 1.

between H1 and N10 atoms, the H₃ImBzim auxiliary ligand takes a rigid planar configuration, as illustrated in Figure 2.

Singlet Excited State Properties: The Calculation of UV–vis Spectrum. The calculated vertical transitions corresponding to the absorption bands are listed in Table 3. The simulated UV–vis absorption bands are reliable. First of all, there are two excitation bands in the investigated energy region. The simulated absorption bands at 426 and 352 nm are in excellent agreement with the experimental value,²⁴ 425 and 350 nm, respectively. Second, the calculated relative intensity of absorption peaks is consistent with the experimental observations (see Table 3). From a quantitative point of view, the computed data are in excellent agreement with the available experimental data for both absorption peaks positions and relative intensities. This confirms, once again, the good performance of TD-DFT and PBE0 xc functional for the description of valence excitations in organometallic Ru(II) complexes.

The two absorption bands are the same in transition character but different in the ways of charge transfer. The first absorption

Table 3. Selected Vertical Excitation in Solution of **1** with Corresponding Energies (in nm), Oscillator Strength (*f*), and Character Assignment

	energy ^a	major contrb.	peaks	<i>f</i>	expt. ^b	assign.
band I	431 nm, 2.878 eV	HOMO → L+2 (76%)	426	0.1353	425 (10070)	MLCT ^c
band II	352 nm, 3.525 eV	H-1 → L+3 (84%)	352	0.4033	350 (18849)	MLCT ^d

^a Only the transitions of interest are indicated. ^b Experimental data see ref 24. Corresponding intensity values are in parentheses, in M⁻¹ cm⁻¹. ^c Metal to H3ImBzim ligand charge transfer transition. ^d Metal to bpy ligand charge transfer transition.

Table 4. Frontier Molecular Orbital Composition of **1** (L = LUMO, H = HOMO, L+1 = LUMO+1, H-1 = HOMO-1, etc.)

MO	composition (%)		
	Ru	bpy	H3ImBzim
L+3	3	87	11
L+2	5	10	86
L+1	11	84	6
LUMO	6	87	7
HOMO	69	9	23
H-1	80	11	9

band (around 426 nm, see Tables 3 and 4) involves metal-to-ligand charge-transfer (MLCT) transition character. Of all of the possible vertical excitations, the excitation of HOMO → L+2 with oscillator strength 0.1353 mainly contributes to the absorption band around 426 nm. On the basis of the frontier molecular orbital (FMO) composition data in Table 4, the MLCT transition at 426 nm can be assigned as the charge transfer from Ru metal center to the H3ImBzim ligand.

The second absorption band (~352 nm) is mainly controlled by the vertical transition from the lower occupied orbital H-1 to the higher virtual orbital L+3. As reported in Table 4, the occupied molecular orbital H-1 is mainly localized on Ru metal with neglectable contribution from bpy ligand (11%) and H3ImBzim ligand (9%). While the virtual molecular orbital L+3 is mastered by bpy ligand with the composition of 87% and a few contribution from H3ImBzim ligand (11%). Thus, the vertical excitation H-1 → L+3 can be assigned as metal Ru to ligand bpy MLCT character with some mixture of intraligand charge-transfer (ILCT) transition localized on H3ImBzim ligand {[9% π(H3ImBzim) → 11% π*(H3ImBzim)]}. In all, the second absorption band is mastered by Ru to bpy ligand MLCT transition with slight interference of H3ImBzim ligand based ILCT transition. In conclusion, the higher energy absorption band is due to the Ru(dπ)-to-bpy(π*) MLCT transition and the lower energy absorptions are mastered by Ru(dπ)-to-H3ImBzim(π*) MLCT transition. This is assignment is reasonable because the π → π* transitions of the H3ImBzim ligand are lower in energy than those of bpy ligand.

Colorimetric Sensor for Anions: Theoretical Understanding. As mentioned earlier, there are two possible mechanisms that control the sensor's response to the F⁻: the hydrogen bonding and deprotonation mechanism. First, we discussed the hydrogen bonding model that the exclusive fluoride sensor should prefer.²⁶ In this case, the F⁻ anions can be attracted to the receptor via the hydrogen-bonding interaction between the NH protons of the coordinated H3ImBzim ligand and F⁻. The fluoride oligomer was not considered in the current investigation. Therefore, the current sensor can grasp three equivalent of F⁻ at most. When 1 equiv of F⁻ was attached to **1**, there are three

possible mathematical configurations. But according to our calculations, no matter what the F⁻ anion in the position near the H2 or H3 proton at the beginning of approaching the sensor, the final configuration would turn into **F2**, as shown in Figure 3. The H2 and H3 protons cannot hold the F⁻ anion alone when there is only 1 equiv of F⁻ to capture. Therefore, there are only two possible configurations when 1 equiv of F⁻ anion is going to attach. Similarly, 2 equiv of F⁻ only produce one possible adduct, **F3**, as shown in Figure 3. There is only one possible configuration of the F⁻ adduct when 3 equiv of F⁻ are involved. But it is noteworthy that the configuration **F4** can only exist if the F-binding process happened in a manner so fast that **1** had no time to fully response to the state of the whole system by polarizing its electron distribution and reorienting itself quickly before the coming of the next F⁻. Theoretically, these configurations can exist because they are free of imaginary harmonic vibrational frequency.

The vertical excitations of these F-binding adducts were explored by the TD-PBE0 approach with basis set II. The simulated absorption spectrum together with the experimental absorption spectrum of **1** are illustrated in Figure 4. As shown in Figure 4, the lower energy absorption band around 426 nm in **1** is red-shifted to 450, 443, 462, and 475 nm in configuration **F1**, **F2**, **F3**, and **F4**, respectively. Whereas in higher energy regions, the change of the absorption band is a bit complicated. The strongest absorption band, 352 nm, in **1** (a) remains unchanged in **F1** (see Figure 4) but; (b) is degenerated into a even higher energy absorption band at 341 nm and a lower energy shoulder absorption band around 382 nm in **F2**; and (c) is red-shifted to 366 and 360 nm in **F3** and **F4**, respectively. In brief, the binding of F⁻ can red-shift the lower energy absorption band but slightly, which does not agree with the obvious red-shift of the lowest energy absorption band, as has been reported experimentally.²⁴ Thus, the observed spectrum change cannot be mastered by the hydrogen-bonding mode.

Before starting the discussion concerning the second F⁻ sensor mechanism in detail, it is worthwhile to figure out the possible pathways in which the deprotonation process can play. We assume that the continuous kinetic deprotonation process can be decomposed into separate steps and the whole process occurs along the lowest energy surface. There are three distinguishable NH protons of the coordinated H3ImBzim ligand. Due to the different chemical environment of these NH protons and the above assumption, theoretically, there are possibly six pathways to deprotonate these protons: (a) H1–H2–H3 (deprotonate H1 first, then H2, and finally H3, etc.); (b) H1–H3–H2; (c) H2–H1–H3; (d) H2–H3–H1; (e) H3–H2–H1; and (f) H3–H1–H2. The energies (Δ*E*) needed to deprotonate the three protons step-by-step are reported in Table 5. From the energy point of view, pathway d, H2–H3–H1, is the easiest way to deprotonate the protons one by one. For clarity, the deprotonated products giving out via pathway d, H2–H3–H1, are denoted as **D1**, **D2**, and **D3**, respectively. Due to the strong hydrogen-bonding interaction between H1 and N10

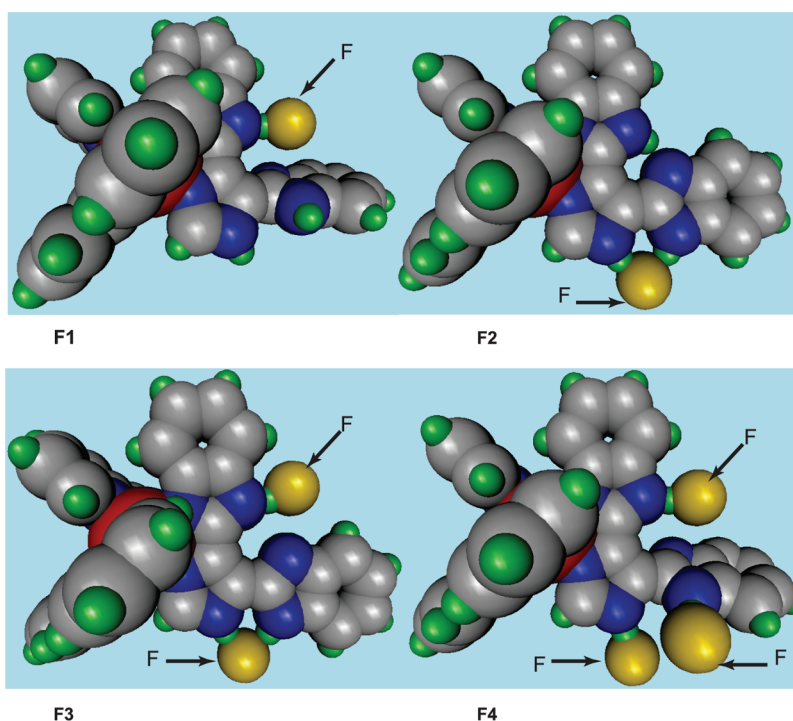


Figure 3. Optimised structures of F-binding adducts in solvent at PBE0/LanL2DZ level.

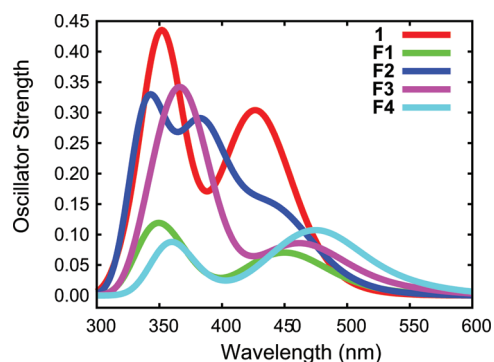


Figure 4. Affection upon absorption spectrum of **1** caused by hydrogen-bonding of F^- .

atoms, more energy is needed to deprotonate H1 proton among the three NH protons. As illustrated in Figure 5, when the NH protons of the coordinated $H_3ImBzim$ deprotonate one-by-one, the absorption bands are progressively red-shifted. The original MLCT peak at 426 nm in **1** is red-shifted to 504 nm upon all the three NH protons were deprotonated completely, meanwhile the strongest MLCT absorption band at 352 nm in **1** is red-shifted to a weak absorption band at 415 nm, eventually. It can be noted that this significant red-shift of the lower energy absorption band upon deprotonation is in agreement with the significant band shift reported in experiment²⁴ when the $[(bpy)_2Ru(H_3ImBzim)]^{2+}$ complex is exposed to F^- anion. The deprotonation increases the electron density of the metal-coordinated $ImBzim^{3-}$, resulting in the decrease of the MLCT band energy, especially the MLCT absorption band mastered by $H_3ImBzim$ ligand.

The change of the absorption intensity should be noted. Compared with **1**, the absorption intensity of **F1**, **F4**, and **D3**

Table 5. Energies (ΔE , in Hartree) Needed to Deprotonate Protons via Different Pathways, PBE0 with Basiset II

steps	a	b	c	d	e	f
1	0.474	0.474	0.448	0.448	0.461	0.461
2	0.460	0.473	0.486	0.484	0.471	0.485
3	0.498	0.485	0.498	0.500	0.500	0.485

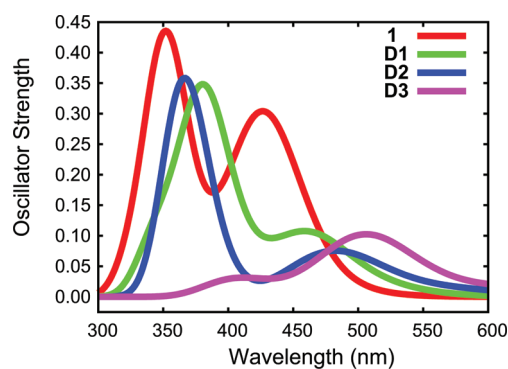


Figure 5. Deprotonation affection upon absorption spectrum.

significantly decreased due to the absence of the hydrogen-binding interaction between H1 and N10. When the H1 proton is attached by F^- or deprotonated away, there is no hydrogen-binding interaction that exists to maintain the planar configuration of $H_3ImBzim$ ligand, resulting in the rotation of the Benzim ring around the C3–C4 bond, which definitely destroys the rigidity of the original $H_3ImBzim$ ligand. Thus, the weak absorption intensity of **D4**, the final deprotonated form of **1**, is reasonable.

CONCLUSIONS

In this work, we explored the electronic properties of the ground state and singlet excited state of a newly developed mixed-ligand transition metal complex $[(byp)_2Ru(H_2ImBzim)]^{2+}$, and discussed its nature for detecting F^- anion with a density functional theory based approach. The following conclusions can be drawn. First, the PBE0 exchange-correlation functional can provide better agreement with the experimental value for the current system. Second, both absorption bands of **1** can be assigned as metal-to-ligand charge transfer (MLCT) transition characters but different in the direction of charge transfer. The higher energy absorption band is mastered by $Ru(d\pi)$ -to- $bpy-(\pi^*)$ MLCT transition while the lower energy absorption band at 426 nm is contributed by the $Ru(d\pi)$ -to- $H_2ImBzim(\pi^*)$ MLCT transition. Finally, the detection ability of the newly developed sensor, $[(byp)_2Ru(H_2ImBzim)]^{2+}$, is based on the proton-transfer model, which makes **1** not only capable of detecting fluoride, but also for the other Bønster base anions. The proton-transfer model explains the experimental observation that the other Bønster base anions, such as AcO^- and $H_2PO_4^-$, can trigger the similar absorption spectrum change as F^- does but different in color. The extent of deprotonation and the corresponding electronic properties of the deprotonation products are responsible for the observed spectral changes. Compared with the other popular organic sensors, the long lifetime and the proton-transfer model gives **1** broad application prospects in the lifetime-based detections. By using the theoretical methods, we explained the experimental phenomena thoroughly and we hope the current exploration can give insight and understanding for sensor preparation.

AUTHOR INFORMATION

Corresponding Author

*E-mail: bhxia@jlu.edu.cn (B.-H.X.); zhanghx@mail.jlu.edu.cn (H.-X.Z).

ACKNOWLEDGMENT

This work was supported by the Natural Science Foundation of China (Grant Nos. 20973076 and 21003057).

REFERENCES

- (1) Gale, P.; García-Garrido, S.; Garric, J. *Chem. Soc. Rev.* **2008**, 37, 151–190.
- (2) Caltagirone, C.; Gale, P. *Chem. Soc. Rev.* **2009**, 38, 520–563.
- (3) Gale, P. A. *Coord. Chem. Rev.* **2006**, 250, 2917–2917.
- (4) Gale, P. A. *Coord. Chem. Rev.* **2003**, 240, 226.
- (5) Sessler, J.; Davis, J. *Acc. Chem. Res.* **2001**, 34, 989–997.
- (6) Lin, T.-P.; Chen, C.-Y.; Wen, Y.-S.; Sun, S.-S. *Inorg. Chem.* **2007**, 46, 9201–9212.
- (7) Chow, C.; Chiu, B.; Lam, M.; Wong, W. J. *Am. Chem. Soc.* **2003**, 125, 7802–7803.
- (8) Lee, D. H.; Im, J. H.; Son, S. U.; Chung, Y. K.; Hong, J.-I. *J. Am. Chem. Soc.* **2003**, 125, 7752–7753.
- (9) Amendola, V.; Esteban-Gómez, D.; Fabbri, L.; Licchelli, M. *Acc. Chem. Res.* **2006**, 39, 343–353.
- (10) Pérez, J.; Riera, L. *Chem. Soc. Rev.* **2008**, 37, 2658–2667.
- (11) Lam, S.-T.; Zhu, N.; Yam, V. W.-W. *Inorg. Chem.* **2009**, 48, 9664–9670.
- (12) Liu, T.; Zhang, H.-X.; Zhou, X.; Zheng, Q.-C.; Xia, B.-H.; Pan, Q.-J. *J. Phys. Chem. A* **2008**, 112, 8254–8262.
- (13) Aaseth, J.; Shimshi, M.; Gabrilove, J.; Birketvedt, G. J. *Trace Elem. Med. Biol.* **2004**, 17, 83–92.
- (14) Cartona, R. *Review of the 2006 United States National Research Council report: Fluoride in drinking water*; Technical Report, 2006.
- (15) Fawell, J.; Bailey, K. *Fluoride in Drinking-Water*; World Health Organization, IWA Publishing: London, U.K., 2006.
- (16) Snowden, T. S.; Anslyn, E. V. *Curr. Opin. Chem. Biol.* **1999**, 3, 740–746.
- (17) Kubo, Y.; Yamamoto, M.; Ikeda, M.; Takeuchi, M.; Shinkai, S.; Yamaguchi, S.; Tamao, K. *Angew. Chem., Int. Ed.* **2003**, 42, 2036–2040.
- (18) Esteban-Gómez, D.; Fabbri, L.; Licchelli, M. *J. Org. Chem.* **2005**, 70, 5717–5720.
- (19) Xie, P.-H.; Guo, F.-Q.; Wang, W.-F.; Liu, X.-Y. *Chem. Pap.* **2010**, 64, 723–728.
- (20) Quang, D. T.; Kim, J. S. *Chem. Rev.* **2010**, 110, 6280–6301.
- (21) Perez, J.; Riera, L. *Chem. Commun.* **2008**, 533–543.
- (22) Yam, V. W.-W. *Acc. Chem. Res.* **2002**, 35, 555–563.
- (23) Demas, J. N.; DeGraff, B. A. *Coord. Chem. Rev.* **2001**, 211, 317–351.
- (24) Saha, D.; Das, S.; Bhaumik, C.; Dutta, S.; Baitalik, S. *Inorg. Chem.* **2010**, 49, 2334–2348.
- (25) Steiner, T. *Angew. Chem., Int. Ed.* **2002**, 41, 48–76.
- (26) Wade, C. R.; Broomsgrove, A. E. J.; Aldridge, S.; Gabba, F. P. *Chem. Rev.* **2010**, 110, 3958–3984.
- (27) Frisch, M. J.; Trucks, G. W.; Schlegel, H. B.; Scuseria, G. E.; Robb, M. A.; Cheeseman, J. R.; Zakrzewski, V. G.; Montgomery, J. A., Jr.; Stratmann, R. E.; Burant, J. C.; Dapprich, S.; Millam, J. M.; Daniels, A. D.; Kudin, K. N.; Strain, M. C.; Farkas, O.; Tomasi, J.; Barone, V.; Cossi, M.; Cammi, R.; Mennucci, B.; Pomelli, C.; Adamo, C.; Clifford, S.; Ochterski, J.; Petersson, G. A.; Ayala, P. Y.; Cui, Q.; Morokuma, K.; Malick, D. K.; Rabuck, A. D.; Raghavachari, K.; Foresman, J. B.; Cioslowski, J.; Ortiz, J. V.; Stefanov, B. B.; Liu, G.; Liashenko, A.; Piskorz, P.; Komaromi, I.; Gomperts, R.; Martin, R. L.; Fox, D. J.; Keith, T.; Al-Laham, M. A.; Peng, C. Y.; Nanayakkara, A.; Gonzalez, C.; Challacombe, M.; Gill, P. M. W.; Johnson, B. G.; Chen, W.; Wong, M. W.; Andres, J. L.; Head-Gordon, M.; Replogle, E. S.; Pople, J. A. *Gaussian 09 Revision A.02*, Gaussian Inc.: Wallingford CT, 2009.
- (28) Kohn, W.; Sham, L. J. *Phys. Rev.* **1965**, 140, A1133–A1138.
- (29) Parr, R. G. *Annu. Rev. Phys. Chem.* **1983**, 34, 631–656.
- (30) Adamo, C.; Barone, V. *J. Chem. Phys.* **1999**, 110, 6158.
- (31) Perdew, J. P.; Burke, K.; Ernzerhof, M. *Phys. Rev. Lett.* **1997**, 78, 1396–1396.
- (32) Perdew, J. P.; Burke, K.; Ernzerhof, M. *Phys. Rev. Lett.* **1996**, 77, 3865–3868.
- (33) Hay, P. J.; Wadt, W. R. *J. Chem. Phys.* **1985**, 82, 299–310.
- (34) Hay, P. J.; Wadt, W. R. *J. Chem. Phys.* **1985**, 82, 270–283.
- (35) Wadt, W.; Hay, P. J. *J. Chem. Phys.* **1985**, 82, 284.
- (36) Dolg, M.; Stoll, H.; Preuss, H.; Pitzer, R. M. *J. Phys. Chem.* **1993**, 97, 5852–5859.
- (37) Schuchardt, K. L.; Didier, B. T.; Elsethagen, T.; Sun, L.; Gurumoorhi, V.; Chase, J.; Li, J.; Windus, T. L. *J. Chem. Inf. Model.* **2007**, 47, 1045–1052, PMID: 17428029.
- (38) Feller, D. *J. Comput. Chem.* **1996**, 17, 1571–1586.
- (39) Guillon, T.; Boggio-Pasqua, M.; Alary, F.; Heully, J.-L.; Lebon, E.; Sutra, P.; Igau, A. *Inorg. Chem.* **2010**, 49, 8862–8872.
- (40) Dunning, T., Jr. *J. Chem. Phys.* **1989**, 90, 1007.
- (41) Casida, M. E.; Jamorski, C.; Casida, K. C.; Salahub, D. R. *J. Chem. Phys.* **1998**, 108, 4439–4449.
- (42) Stratmann, R. E.; Scuseria, G. E.; Frisch, M. J. *J. Chem. Phys.* **1998**, 109, 8218–8224.
- (43) Walters, V. A.; Hadad, C. M.; Thiel, Y.; Colson, S. D.; Wiberg, K. B.; Johnson, P. M.; Foresman, J. B. *J. Am. Chem. Soc.* **1991**, 113, 4782–4791.
- (44) Cossi, M.; Scalmani, G.; Rega, N.; Barone, V. *J. Chem. Phys.* **2002**, 117, 43–54.
- (45) Barone, V.; Cossi, M.; Tomasi, J. *J. Chem. Phys.* **1997**, 107, 3210–3221.
- (46) Mennucci, B.; Tomasi, J. *J. Chem. Phys.* **1997**, 106, 5151–5158.
- (47) Caricato, M.; Mennucci, B.; Tomasi, J.; Ingrosso, F.; Cammi, R.; Corni, S.; Scalmani, G. *J. Chem. Phys.* **2006**, 124, 124520.

- (48) Mennucci, B.; Cappelli, C.; Guido, C. A.; Cammi, R.; Tomasi, J. *J. Phys. Chem. A* **2009**, *113*, 3009–3020.
- (49) O'boyle, N.; Tenderholt, A.; Langner, K. *J. Comput. Chem.* **2008**, *29*, 839–845.
- (50) Dreuw, A.; Head-Gordon, M. *Chem. Rev.* **2005**, *105*, 4009–4037.
- (51) Li, X.-N.; Liu, X.-J.; Wu, Z.-J.; Zhang, H.-J. *J. Phys. Chem. A* **2008**, *112*, 11190–11197.
- (52) Li, X.-N.; Wu, Z.-J.; Liu, X.-J.; Zhang, H.-J. *J. Phys. Chem. A* **2010**, *114*, 9300–9308.
- (53) Li, X.-N.; Wu, Z.-J.; Si, Z.-J.; Zhang, H.-J.; Zhou, L.; Liu, X.-J. *Inorg. Chem.* **2009**, *48*, 7740–7749.
- (54) Jacquemin, D.; Perpète, E. A.; Ciofini, I.; Adamo, C. *Acc. Chem. Res.* **2009**, *42*, 326–334.
- (55) Tognetti, V.; Floch, P. L.; Adamo, C. *J. Comput. Chem.* **2009**, *31*, 1053–1062.
- (56) Lee, C.; Yang, W.; Parr, R. G. *Phys. Rev. B* **1988**, *37*, 785–789.
- (57) Becke, A. D. *J. Chem. Phys.* **1993**, *98*, 5648–5652.
- (58) Lide, D. R. *CRC Handbook of Chemistry and Physics*, 85th ed.; National Institute of Standards & Technology (Retired): Gaithersburg, Maryland, USA, 2004.